Thermal-wave nondestructive evaluation of cylindrical composite structures using frequency-domain photothermal radiometry

Chinhua Wang,[a] Andreas Mandelis, and Yue Liu
Center for Advanced Diffusion Wave Technologies, Department of Mechanical and Industrial Engineering, University of Toronto, Ontario M5S 3G8, Canada

(Received 7 July 2004; accepted 23 September 2004; published online 16 December 2004)

In this paper, thermal-wave diagnostics by means of laser infrared photothermal radiometry (PTR) have been used for quantitative nondestructive evaluation of cylindrical composite structures. To quantitatively evaluate the thermal-wave field of a cylindrical composite material, the Green function corresponding to the composite structure and the PTR measurement scheme has been developed and subsequently the thermal-wave field has been derived. Furthermore, the characteristics of the thermal-wave field for two cases of practical interest, i.e., a cylindrical material with a surface coating and a cylindrical tube filled with a low thermal-conductivity fluid medium inside, are discussed. Experimental results from a stainless-steel (AISI 302) cylinder are used to validate the theoretical model. © *2005 American Institute of Physics*. [DOI: 10.1063/1.1819999]

I. INTRODUCTION

Photothermal techniques, including photoacoustics (PA), photothermal radiometry (PTR), and photothermal deflection (PTD), have become powerful tools for the thermophysical characterization and nondestructive evaluation (NDE) of various materials in the past few decades.[1–5] In all of these applications of the photothermal techniques, measurement of thermophysical properties and/or detection of defect structures is based on the thermal-wave fields inside the samples which ultimately depend on a few important factors, such as optical excitation scheme (using either an expanded beam, 1D limit, or a focused beam, 3D limit), sample materials (homogeneous or inhomogeneous), and sample geometry (plane or curved surface). The rapid development of photothermal techniques has allowed the evaluation not only of homogeneous materials[5] but also of layered and/or buried structures[6] using either a planar or a pointlike thermal-wave excitation source. However, research using all current photothermal techniques so far has been mainly focused on samples with flat surfaces although some attempts have been made to evaluate cylindrical or spherical subsurface defect structures lying below a flat surface.[4,5] Very recently, the PTR technique was extended to the study of homogeneous cylindrical (curved surface) materials, in which both theoretical model and experimental validation were performed[7] on steel rod samples. Motivated by the growing interest in applying photothermal methods to composite industrial cylindrical samples, in this paper we extend the PTR technique to the study of inhomogeneous (layered) cylindrical structures. Specifically, we present both theoretical and experimental PTR studies on metallic-layered cylindrical samples. Based on the Green-function method,[8] the oscillating temperature (thermal-wave field) of the cylindrical surface under photothermal excitation by a periodically modulated spatially uniform beam is obtained and the theoretical model is further validated by experiments. It is expected that the study of cylindrical composite structures is especially useful for characterization and nondestructive evaluation of materials, such as cylinders with coatings, hollow tubes, and/or case-hardened steels such as screws and nails, to name a few. This is so because most of these cylindrical-type products usually undergo industrial processing, such as heat treatment, after manufacturing. Although the properties of the bulk material, of which such products are made, can be known, the properties of the products, especially the properties of the surface layer change significantly after the heat treatment. Given that there is an increasing industrial interest in characterizing the surface layer, the deviation of its thermophysical properties from those of the untreated material can be used for nondestructive monitoring of the effects of processing (e.g., heat treating) on the sample. Moreover, this technique can also be useful in the nondestructive thickness evaluation of coatings on cylindrical samples, if the properties of the coating and the cylindrical sample are known. The paper is organized as follows. We first work out an appropriate Green function suitable for the PTR measurement scheme; then we present an analytical expression for the thermal-wave field, followed by discussion of the physical behavior of the PTR signal. Finally, experimental results are presented and compared to the theory to validate the model.

II. THEORY

The thermal-wave field in an infinitely long composite cylindrical sample consisting of two concentric regions of radii a (region I) and b (region II) can be derived based on the Green-function method. The thermal conductivity and diffusivity of regions I and II are denoted with (k_1, α_1) and (k_2, α_2), respectively. The geometry and the coordinates of the boundary-value problem are shown in Fig. 1.

The composite cylindrical solid is externally excited by a uniform-intensity laser beam of infinite extent in the direction perpendicular to the plane of the paper in Fig. 1, which represents a transverse cross section of the infinitely long solid. The beam is assumed to be perfectly collimated along

[a]Electronic mail: chwang@mie.utoronto.ca

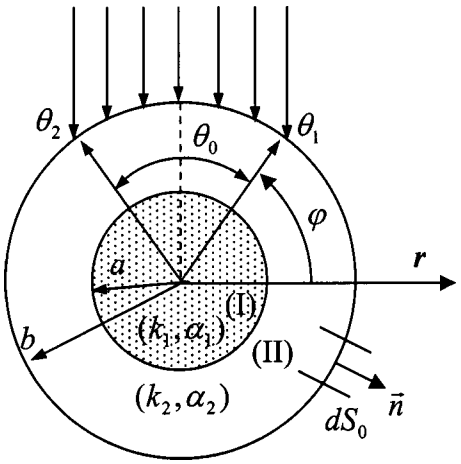

FIG. 1. Cross section of an infinitely long composite cylinder consisting of two concentric regions of radii a (region I) and b (region II) under external illumination by a uniform light beam impinging on part of its surface subtending a sector of angle θ_0.

the axial direction and subtending a sector of angle θ_0. Due to the nature of the radiometric signal (Planck radiation) from opaque solids such as metals and coatings, only the oscillating temperature of the external surface of the cylinder is of interest. To obtain an expression for the thermal-wave field on the surface, the governing thermal-wave equation for region II must be solved. Considering harmonic modulation of the incident exciting light, the thermal-wave equation for region II can be written as

$$\nabla^2 T(\mathbf{r},\omega) - \sigma_2{}^2(\omega) T(\mathbf{r},\omega) = -\frac{1}{k_2} Q(\mathbf{r},\omega), \tag{1}$$

where $\sigma_2(\omega) = (i\omega/\alpha_2)^{1/2} = (1+i)\sqrt{\omega/2\alpha_2}$ is the thermal wave number in region II, ω is the angular modulation frequency, and $Q(\mathbf{r},\omega)$ is the volume thermal source at coordinates (r,φ) in region II of the material. Based on the Green-function method, the general solution for Eq. (1) can be expressed as[8]

$$\begin{aligned} T(r,\omega) = (\alpha_2/k_2) &\int\int\int_{V_0} Q(\mathbf{r}_0,\omega) G(\mathbf{r}|\mathbf{r}_0;\omega) dV_0 \\ &+ \alpha_2 \oint_{S_0} [G(\mathbf{r}|\mathbf{r}_0^s;\omega) \nabla_0 T(\mathbf{r}_0^s;\omega) \\ &- T(\mathbf{r}_0^s,\omega) \nabla_0 G(\mathbf{r}|\mathbf{r}_0^s;\omega)] d\mathbf{S}_0, \end{aligned} \tag{2}$$

where S_0 is the entire surface (including S_2, the exterior surface at $r=b$, and S_1, the interior interface at $r=a$) surrounding the domain volume V_0 (i.e., region II) which includes the harmonic source $Q(\mathbf{r}_0,\omega)$. $\mathbf{r}_0^s$ is the source coordinate point in the bulk or on surface S_0. $d\mathbf{S}_0$ indicates an infinitesimal area vector along the outward direction normal to the boundary surface S_0: $d\mathbf{S}_0 = \mathbf{n} dS_0$ with $\mathbf{n}$ being the outward unit vector, as shown in Fig. 1. $G(\mathbf{r}|\mathbf{r}_0;\omega)$ is the Green function which takes different forms depending on the types of the homogeneous boundary conditions, either Dirichlet, Neumann, or third kind, imposed on the investigated region II.

As discussed elsewhere,[7,8] Eq. (2) gives the most general formula to evaluate the thermal-wave field in the region under investigation. However, in most cases, Eq. (2) can be simplified depending on specific material properties and boundary conditions imposed on the solid. For solids with high attenuation of the incident light, such as metallic samples, the absorption of the incident light occurs at the surface, and therefore, the volume source can be neglected. In this paper, we will focus on opaque materials. Moreover, considering that illumination of the external surface by a laser beam leads to optical-to-thermal energy conversion essentially at the surface and that the thermal coupling (loss) coefficient between a metallic solid and the surrounding gas (air) is on the order of 10^{-3},[9] the adiabatic second-kind (Neumann) boundary condition at the external surface can be applied. Furthermore, to convert the proper Green function (i.e., one with homogeneous boundary conditions) to an improper one which can be applied to multilayered solids with nonhomogeneous interface conditions, we assume a third-kind boundary condition (general case) on the interior surface of region II (i.e., at $r=a$).[8] The homogeneous boundary conditions for the appropriate Green function and inhomogeneous boundary conditions for the temperature field, respectively, can be written as

$$k_2 \left.\frac{\partial}{\partial n} G(\mathbf{r}|\mathbf{r}_0;\omega)\right|_{r_0=a} = h_1 G(a|\mathbf{r}_0;\omega), \tag{3a}$$

$$k_2 \left.\frac{\partial}{\partial n} G(\mathbf{r}|\mathbf{r}_0;\omega)\right|_{r_0=b} = 0, \tag{3b}$$

$$-k_2 \left.\frac{\partial}{\partial n} T(\mathbf{r}_0,\omega)\right|_{r_0=a} = F_1(\mathbf{r}_0,\omega)|_{r_0=a} - h_1 T(|\mathbf{r}_0;\omega)|_{r_0=a}, \tag{4a}$$

$$k_2 \left.\frac{\partial}{\partial n} T(\mathbf{r}_0,\omega)\right|_{r_0=b} = F_2(\mathbf{r}_0,\omega)|_{r_0=b}, \tag{4b}$$

where h_1 [W m^{-2} K^{-1}] is the heat transfer coefficient at the inner surface S_1. F_1 and F_2 are the heat fluxes (W m^{-2}) imposed on the interior and the exterior surface, respectively. Therefore, in the absence of volume thermal sources in region II and in the underlying region I, and with the homogeneous boundary conditions for the Green function shown in Eqs. (3) and (4), the general thermal-wave field represented by Eq. (2) reduces for an axially infinitely long cylinder to

$$\begin{aligned} T(r,\varphi,\omega) = &-(\alpha_2/k_2) \oint_{S_1} F_1(\mathbf{r}_0,\omega) G(\mathbf{r}|\mathbf{r}_0;\omega) d\mathbf{S}_0 \\ &+ (\alpha_2/k_2) \oint_{S_2} F_2(\mathbf{r}_0,\omega) G(\mathbf{r}|\mathbf{r}_0;\omega) d\mathbf{S}_0, \end{aligned} \tag{5}$$

where $G(\mathbf{r}|\mathbf{r}_0;\omega)$ is the Green function for region II which must be derived so as to satisfy the appropriate boundary conditions. It should be emphasized that the condition for Eq. (2) to be reduced to Eq. (5) is that the Green function must be proper (i.e., homogeneous boundary conditions must be satisfied at all surfaces enclosing the volume V_0).

The details of the derivation of the Green function for the specified geometry are given in the Appendix. Section I of the Appendix gives the Green function and the spatial

impulse-response function in region II and I, respectively, for a two-layer concentric cylindrical structure. The relevant Green function to be used in the exterior region $a \leqslant r \leqslant b$ is Eq. (A1.23). In the interior region $0 \leqslant r \leqslant a$, the spatial impulse-response function $H(\mathbf{r},\mathbf{r}_0;\omega)$, Eq. (A1.24), which is *not* a Green function, must be used instead. However, great care must be taken since the Green-function derivation for region II has employed a nonhomogeneous (continuity) boundary condition at $r=a$. Therefore, the function Eq. (A1.23) is an improper Green function. As a result, it cannot be applied readily to obtain the thermal-wave field in region II, because it does not satisfy the requisite homogeneous boundary condition at $r=a$ to validate the field Eq. (5). A *proper* Green function for the *equivalent* exterior region II, which satisfies a homogeneous third-kind boundary condition at $r=a$, must be used instead. This Green function is given in Eq. (A2.16). However, in Eq. (A2.16) there is no direct thermal-wave coupling to the underlayer in region I; there is only an indirect involvement of the inner region at thermal equilibrium through the heat transfer coefficient h_1. A direct involvement of region I into the proper Green function for region II, Eq. (A2.16), can be introduced through correlating the thermal parameters (k_1,α_1) in the impulse-response Eq. (A1.23) in region II to the (otherwise arbitrary) constant h_1 in Eq. (A2.16). This line of reasoning leads to the *equivalence relations* (A3.3) and (A3.4) in Sec. III of the Appendix. Those relations show that for the specified value of h_1, the proper Green function Eq. (A2.16), and its integral, Eq. (5), can be used as an equivalent Green function and as a valid thermal-wave field distribution integral, respectively, to describe the effects of the double layer, despite the nonhomogeneous interior boundary conditions. In summary, the appropriate Green function to be used in Eq. (5) can finally be written with the observation coordinate, r, as the running variable in the form

$$G(\mathbf{r}|\mathbf{r}_0;\omega)=\frac{1}{2\pi\alpha_2}\sum_{m=-\infty}^{\infty}\frac{e^{im(\varphi-\varphi_0)}}{[Y_m(b)-X_m(a)]} \times\begin{cases} K_m(\sigma_2 r_0)[K_m(\sigma_2 r)-X_m(a)I_m(\sigma_2 r)]-Y_m(b)I_m(\sigma_2 r_0)[K_m(\sigma_2 r)-X_m(a)I_m(\sigma_2 r)] & (a\leqslant r\leqslant r_0)\\ K_m(\sigma_2 r)[K_m(\sigma_2 r_0)-X_m(a)I_m(\sigma_2 r_0)]-Y_m(b)I_m(\sigma_2 r)[K_m(\sigma_2 r_0)-X_m(a)I_m(\sigma_2 r_0)] & (r_0\leqslant r\leqslant b)\end{cases} \tag{6}$$

where $I_m(z)$, $K_m(z)$ are the complex-argument modified Bessel functions of the first kind and of the second kind of order m, respectively, and

$$X_m(a)\equiv\frac{K_m'(\sigma_2 a)-\eta_{1m}K_m(\sigma_2 a)}{I_m'(\sigma_2 a)-\eta_{1m}I_m(\sigma_2 a)}\quad(m=0,1,2\ldots), \tag{7}$$

$$Y_m(b)\equiv\frac{K_m'(\sigma_2 b)}{I_m'(\sigma_2 b)}\quad(m=0,1,2\ldots), \tag{8}$$

$$\eta_{1m}\equiv\frac{I_m'(\sigma_1 a)}{\beta_{21}I_m(\sigma_1 a)}\quad(m=0,1,2,\ldots) \tag{9}$$

and

$$\beta_{21}\equiv k_2/k_1. \tag{10}$$

In view of the structure of Eq. (5), the prescribed heat fluxes F_1 and F_2 at the interior and exterior surface, respectively, must be specified. In our case, there is no incident heat flux prescribed at the interior surface $r=a$, therefore,

$$F_1(a,\varphi_0,\omega)=0. \tag{11}$$

Assuming that the incident light intensity on the exterior surface is uniform, in conformity with our experimental PTR configuration, the thermal-wave flux on that surface must be weighted using a projection factor in the form of the cosine of the incident uniform light intensity which can be expressed as (Fig. 1)

$$F_2(b,\varphi_0;\omega)=\begin{cases}F_0\cos(90^\circ-\varphi_0), & \theta_1\leqslant\varphi_0\leqslant\theta_2\\ 0, & \text{other angles}\end{cases}. \tag{12}$$

Substituting Eq. (12) into Eq. (5), we find

$$T(r,\varphi,\omega)=\frac{\alpha_2 F_0 b}{k_2}\oint_{S_2}G(\mathbf{r}|\mathbf{r}_0;\omega)\cos(90^\circ-\varphi_0)d\varphi_0. \tag{13}$$

Now interchanging $(r,\varphi)\Leftrightarrow(r_0,\varphi_0)$ in the Green function Eq. (6) so as to allow integration over the source coordinates (r_0,φ_0), and letting $r_0=b$ (surface source), Eq. (13) becomes

$$T(r,\varphi,\omega)=\frac{F_0}{2\pi k_2}\int_{\theta_1}^{\theta_2}\sum_{m=-\infty}^{\infty}\frac{K_m(\sigma_2 r)-X_m(a)I_m(\sigma_2 r)}{I_m'(\sigma_2 b)[Y_m(b)-X_m(a)]} \times e^{im(\varphi_0-\varphi)}\cos(90^\circ-\varphi_0)d\varphi_0. \tag{14}$$

Using the identity

$$\sum_{m=-\infty}^{\infty}e^{im(\varphi-\varphi_0)}=1+2\sum_{m=1}^{\infty}\cos[m(\varphi-\varphi_0)] \tag{15}$$

and[10]

$$I_{-\nu}(z)=I_\nu(z)\quad K_{-\nu}(z)=K_\nu(z), \tag{16}$$

after some algebraic manipulation, we finally obtain the thermal-wave field in region II

$$T(r,\varphi,\omega)=\frac{F_0}{2\pi k_2}\left\{2\left(\frac{K_0(\sigma_2 r)-X_0(a)I_0(\sigma_2 r)}{I_0'(\sigma_2 b)[Y_0(b)-X_0(a)]}\right)\sin\frac{\theta_0}{2}+\left(\frac{K_1(\sigma_2 r)-X_1(a)I_1(\sigma_2 r)}{I_1'(\sigma_2 b)[Y_1(b)-X_1(a)]}\right)(\theta_0+\sin\theta_0)\cos\left(\frac{\pi}{2}-\varphi\right)\right.$$
$$\left.+2\sum_{m=2}^{\infty}\left(\frac{K_m(\sigma_2 r)-X_m(a)I_m(\sigma_2 r)}{I_m'(\sigma_2 b)[Y_m(b)-X_m(a)]}\right)\cos\left[\frac{m}{2}(\pi-2\varphi)\right]\left[\frac{\sin[(m+1)\theta_0/2]}{m+1}+\frac{\sin[(m-1)\theta_0/2]}{m-1}\right]\right\}. \quad (17)$$

Here $X_m(a)$ and $Y_m(b)$ $(m=0,1,2\ldots)$ are given in Eqs. (7)–(10). As a check, Eq. (17) can be easily reduced to the single-layer (homogeneous cylinder) model[7] if we set parameters (k_1,α_1) in region I equal to parameters (k_2,α_2) in region II, i.e., $(k_1,\alpha_1)\rightarrow(k_2,\alpha_2)$ in Eqs. (9) and (10).

Equation (17) gives the thermal-wave field at any point inside region II. From the structure of this expression, it is seen that the frequency dependence of the thermal-wave field of cylindrical samples under uniform illumination is a function of the thermophysical properties and geometrical dimensions of both interior and exterior materials, as expected.

III. NUMERICAL SIMULATIONS

Although Eq. (17) explicitly demonstrates the relationship between the thermal-wave field and the thermophysical parameters, as well as several geometric and measurement configuration factors for a composite cylindrical sample of infinite axial extent, the complicated functional dependence of the signal on the various system parameters makes any qualitative attempts for further understanding the system behavior difficult. To gain more physical insight into the characteristics of the ac temperature field, it is instructive to study its dependence on each individual parameter involved in Eq. (17). Although the thermal-wave field can be calculated at any point inside region II, our simulations will be restricted to the sample surface at $r=b$, from which experimental measurement data can be obtained using the PTR technique. In all the simulations, the amplitude and phase of the surface temperature oscillation are normalized to the corresponding amplitude and phase of a flat surface of a semi-infinitely thick sample of the same material as either the interior (region I) or the exterior solid (region II), depending on the sample structure. The procedure of the normalization with a flat surface renders the characteristics of the surface curvature more pronounced, since the common frequency dependencies of the signals from the flat and curved surfaces can be eliminated. In the usual manner, the aforementioned normalizations are performed in the form of the ratio and the difference of the two individual amplitudes and phases, respectively. The amplitude and phase of a flat surface are calculated based on the well-known 1D theoretical model which is valid under the condition that the incident-beam size is much larger than the thermal diffusion length of the material within the modulation frequency range of interest. Under illumination with a constant thermal-wave flux F_0 on the surface of the flat sample, the thermal-wave field evaluated at the surface is given by[11]

$$T(0,\omega)=F_0\left(\frac{\sqrt{\alpha}}{k\sqrt{\omega}}\right)e^{-i\pi/4}, \quad (18)$$

where α and k are the thermal diffusivity and the thermal conductivity of the material, respectively. The thermal-wave field given in Eq. (18) clearly exhibits the well-known dependence of the amplitude on the inverse of the square root of the frequency as well as a constant $(\pi/4)$ phase lag of the temperature oscillation with respect to the incident thermal flux in a semi-infinite solid. The simulations were performed using MATLAB in which the modified Bessel function of the first kind and second kind with complex variables can be calculated directly.

Figure 2 shows the effect of thickness of an aluminum coating on an AISI 1018 steel rod (composition: 0.14%–0.2% C, 0.6%–0.9% Mn) in a composite cylindrical system. In the simulation, the exterior radius b is fixed at $b=1.5$ mm, while the interior radius a is set as a variable parameter. The thermal-wave field is calculated at $\varphi=90°$ (see Fig. 1) and the beam size is assumed to be large enough so as to cover the entire upper part of the cylinder; therefore, $\theta_0=180°$ is assumed in the calculation. The amplitude and phase of the thermal-wave field are normalized by a semi-infinite AISI 1018 steel flat surface. The other parameters used in the simulation are $F_0=1$ W/m^2, $k_1=51.9$ W/m K, $\alpha_1=13.57\times10^{-6}$ m^2/s for AISI 1018 steels,[12] and $k_2=237$ W/m K, $\alpha_2=97.1\times10^{-6}$ m^2/s for aluminum coating.[13] It is seen that with increasing Al coating thickness, both amplitude and phase curves of the composite structure change toward those of a homogeneous aluminum cylinder of the same diameter. When the thickness of the Al coating is small compared to the thermal diffusion length in the coating, the thermal-wave field is dominated by the contribution of the steel substrate. This can be seen in both amplitude and phase curves in the cases of 25- and 100-μm Al coating thicknesses when compared with that of pure 1018 steel rod, especially at the lower frequencies. This can be understood by the larger thermal diffusion length at lower frequencies which results in a signal dominated by the thicker substrate steel. The thermal diffusion length $\mu=\sqrt{\alpha/\pi f}$ for AISI 1018 steel and aluminum at 10 Hz is $\sim$0.76 and 1.76 mm, respectively. The contribution from the surface coating is mainly seen at higher frequencies, at which the thermal-wave field is dominated by the coating material due to the shorter thermal diffusion lengths. This is manifested by the fact that both amplitude and phase curves deviate from those of the pure 1018 steel rod and move toward the aluminum curve. As the coating thickness increases, the contribution from the alumi-

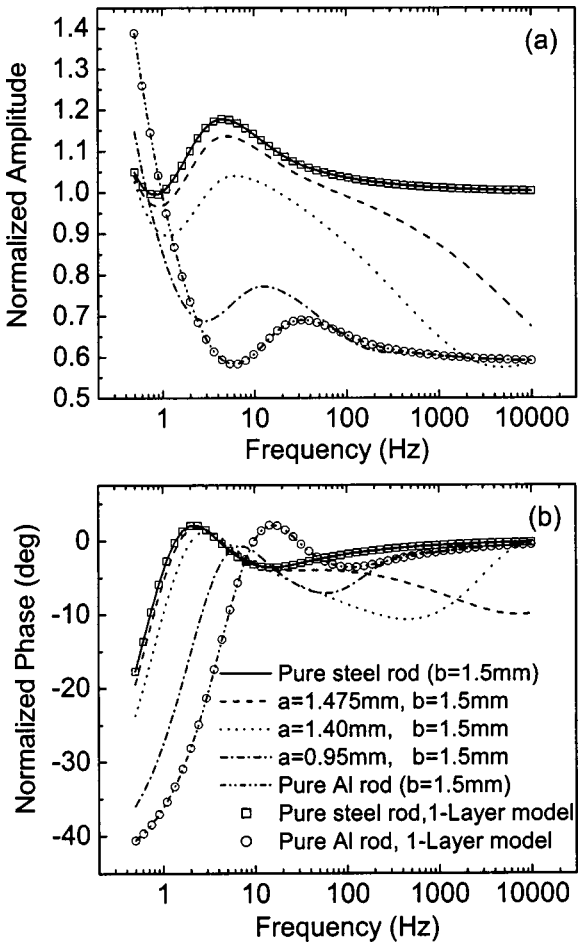

FIG. 2. Effect of thickness of an aluminum coating on an AISI 1018 steel rod in a composite cylindrical structure. The parameters used in the simulation are $F_0=1$ W/m^2, $k_1=51.9$ W/m K, $\alpha_1=13.57\times10^{-6}$ m^2/s for AISI 1018 steels, and $k_2=237$ W/m K, $\alpha_2=97.1\times10^{-6}$ m^2/s for aluminum coating.

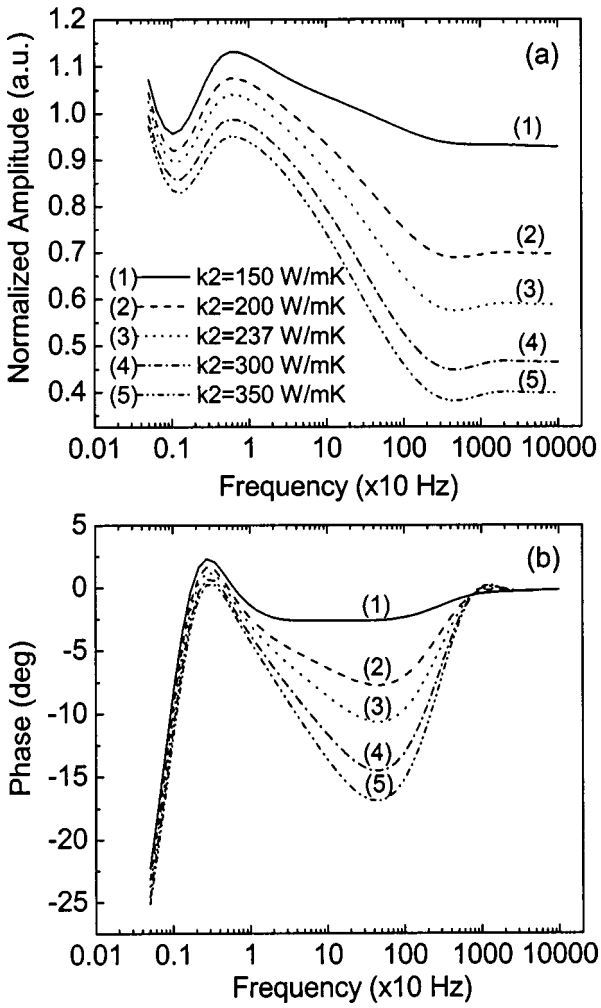

FIG. 3. Effect of the thermal conductivity of an aluminum coating on an AISI 1018 steel rod in a composite cylindrical structure. The radii of the interior solid and full cylinder are $a=1.4$ mm and $b=1.5$ mm, respectively. Thermal diffusivity of the coating $\alpha_2=97.1\times10^{-6}$ m^2/s. $k_1=51.9$ W/m K, $\alpha_1=13.57\times10^{-6}$ m^2/s for AISI 1018 steels.

num coating gradually dominates and ultimately transits to the behavior of a pure aluminum rod. This includes smaller amplitudes, Fig. 1(a), and a shift of the phase interference peak pattern to higher frequencies, Fig. 2(b). As a check, the simulation results using a homogeneous model[7] are also shown in Fig. 2(b) to indicate the consistency of the two models.

Figures 3 and 4 show, respectively, the effects on the thermal-wave field of changing thermal conductivity and thermal diffusivity of the coating, when the coating is relatively thin, i.e., $a=1.4$ mm and $b=1.5$ mm. In the simulation, the surface thermal-wave field is calculated at $\varphi=90°$, with $\theta_0=180°$. The other parameters used for 1018 steel and aluminum coating are the same as above. The amplitude and phase are also normalized with the 1018 steel flat-surface material. In both plots of Figs. 3 and 4, the long "tail" in amplitude at high frequencies and "dip" (lag) in phase at intermediate frequencies are due to the increasing thermal contribution from the coating which is a better conductor and diffuser than the substrate steel, as discussed in Fig. 2. In Fig. 3, it is seen that as the thermal conductivity of the coating increases, the amplitude tail decreases, while the phase lag (i.e., absolute magnitude of the phase) increases, as expected from the domination of the surface thermal-wave field by the coating at higher frequencies (larger than 10 Hz). When the frequency is above 1 kHz, the amplitude changes slope and the phase turns around. This can be explained by the way the data are normalized to the values of the flat sample; at very high frequencies, the curvature will not matter compared to the small diffusion length and the signals will settle at a constant amplitude ratio, as witnessed by the flat parallel curves at $f>10$ kHz in Fig. 3(a) (zero slope) and by the zero phase difference in Fig. 3(b), essentially corresponding to two flat semi-infinite solids made of aluminum and steel, respectively; the phase difference will become zero no matter what the solids are, as per Eq. (18). On the contrary, the normalized amplitude increases, the phase lag decreases, Fig. 4, when the thermal diffusivity of the coating increases. These trends are, at first glance, inconsistent with the expected thermal-wave behavior of the cylindrical solid, but they are the result of assuming in the simulation that thermal diffusivity and conductivity are independent parameters: as can be seen from the simple flat surface Eq. (18), under this independence assumption, the PTR signal is pro-

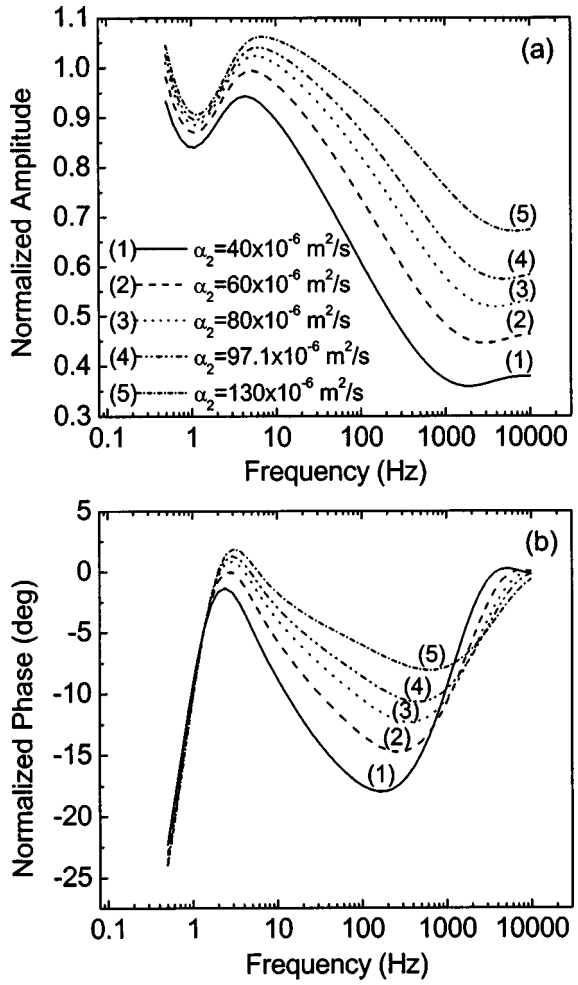

FIG. 4. Effect of the thermal diffusivity of an aluminum coating on an AISI 1018 steel rod in a composite cylindrical structure. The radii of the interior solid and full cylinder are $a=1.4$ mm and $b=1.5$ mm, respectively. Thermal conductivity of the coating $k_2=237$ W/m K. $k_1=51.9$ W/m K, $\alpha_1=13.57\times10^{-6}$ m^2/s for AISI 1018 steels.

portional to $\sqrt{\alpha}$ and inversely proportional to k. The former dependence gives rise to the observed behavior. It will be noted, however, that if the proper dependence of α on k is explicitly accounted for, namely, $\alpha=k/\rho C$, where ρ is the density and C is the specific heat of the material, then $T(0,\omega)\propto 1/k^{1/2}$, as expected intuitively. The same physical situation is encountered with the cylindrical geometry of Eq. (17), albeit with more complicated mathematics. In practice, the main use of these models is for fitting to experimental data and extracting values of the thermal diffusivities and conductivities. In the fits, the two thermophysical parameters are taken as independent quantities and for this reason, it is valuable to study their effects on the thermal-wave behavior independently. Furthermore, as the thermal conductivity of the coating changes, Fig. 3, the positions of the phase thermal-wave interference extrema (peak and dip) remain essentially unchanged, while the same positions change significantly as the thermal diffusivity changes, Fig. 4. This is the result of the fact that thermal diffusivity contributes to the thermal-wave field as the bulk transport parameter, controlling the subsurface position of the heat centroid,[11] whereas conductivity simply controls the overall magnitude of the field. Therefore, field dependence on the former is a much more sensitive function of coating thickness than on the latter. This behavior is of particular significance for measuring thermal diffusivity of the coating from the peak-to-trough position change in the phase plot, provided the coating thickness is known, or vice versa. To measure α_2 without exact knowledge of the k_2 value, one may assign a plausible k_2 value, since, from Fig. 3, that value does not change the thermal-wave interference-related relative maximum-to-minimum distance on the frequency axis in either amplitude or phase channel. On the other hand, from Fig. 4, changes in α_2 cause changes in that distance in both amplitude and phase. Therefore, the α_2 value can be calibrated from that measurement and easily obtained for practical applications of the technique.

In the foregoing discussion, the interior material and the coating have thermal conductivities of the same or similar order of magnitude and the surface thermal-wave field is determined by both the interior and exterior materials depending on the diameter of the cylinder and the thickness of the coating. In practice, another special category of the two-layer cylindrical composite structure of considerable importance is a cylindrical tube or pipe. In this case, the thermal-wave field is determined by the tube material only, with negligible contribution from the fluid or gas inside. For a metallic tube filled with either air (hollow) or low thermal-conductivity fluids, the thermal-conductivity ratio given in Eq. (10) is usually very large.

$$\beta_{21}=k_2/k_1\approx 10^2\ \mathrm{W\,m^{-1}\,K^{-1}}/(10^{-2}-10^{-1})\mathrm{W\,m^{-1}\,K^{-1}}$$
$$\rightarrow 10^3-10^4.$$

As a result, $\eta_{1m}\rightarrow 0$, Eq. (9), which implies that the thermal-wave field is more or less confined within the exterior region and is determined by the interior and exterior diameters and the thermal diffusivity of the tube material only. Figure 5 shows the effect on the thermal-wave field of the thickness of a copper tube as the tube wall, calculated using either the approximate formula with $\eta_{1m}=0$ in Eq. (17) or the full formula. The tube was assumed to be filled with air. As above, the calculation was made using $\varphi=90°$ and $\theta=180°$. The other parameters used in the simulation are $\alpha_2=117\times10^{-6}$ m^2/s, $k_2=401$ W/m K for copper[13] and $\alpha_1=22.5\times10^{-6}$ m^2/s, $k_1=0.0263$ W/m K for air.[13] The exterior diameter of the tube was fixed at $2b=4.7$ mm. The amplitude and phase were normalized with those from a semi-infinite copper material with a flat surface. As a reference, the thermal-wave field of a solid copper cylinder is also shown in the plot. It is seen from Fig. 5(a) that the normalized amplitude increases rapidly at lower frequencies as the wall thickness of the tube decreases, representing a rapid departure from the solid copper cylinder with enhanced thermal-wave confinement within the copper tube. At higher frequencies, the thermal diffusion length becomes shorter and the walls of the copper tube become "thermally thick,"[11] thus shifting the normalized amplitude toward unity, as expected. In Fig. 5(b) the phase exhibits increased thermal-wave interference character with decreasing wall thickness and the interference

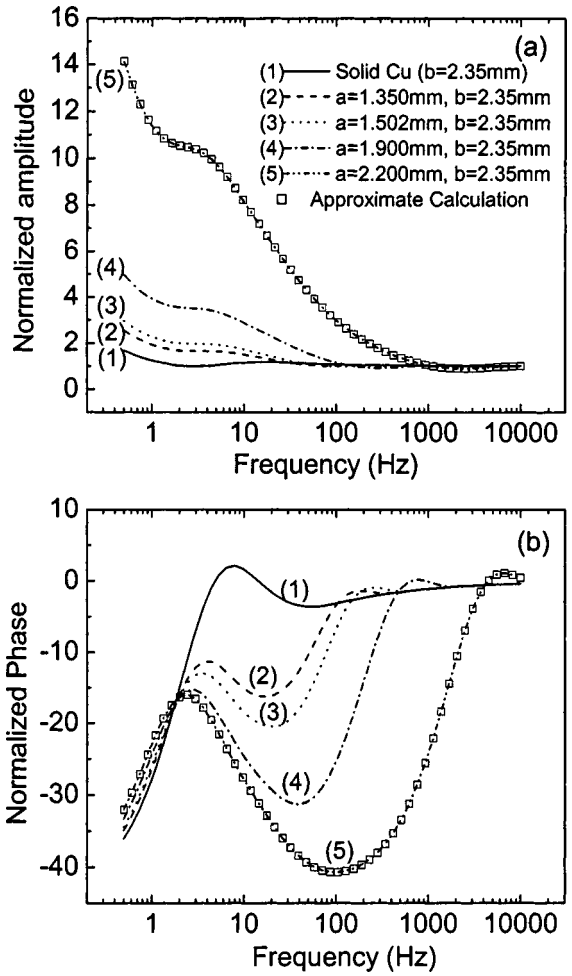

FIG. 5. Effect of the wall thickness of a copper tube on the thermal-wave field, calculated using either an approximate formula [$\eta_{1m}=0$ in Eq. (17)—black squares) or the full Eq. (17)—solid or dashed line]. The tube is filled with air. The parameters used in the simulation are $\alpha_2=117\ \mathrm{m}^2/\mathrm{s}$, $k_2=401\ \mathrm{W/m\,K}$ for copper and $\alpha_1=22.5\times10^{-6}\ \mathrm{m}^2/\mathrm{s}$, $k_1=0.0263\ \mathrm{W/m\,K}$ for air.

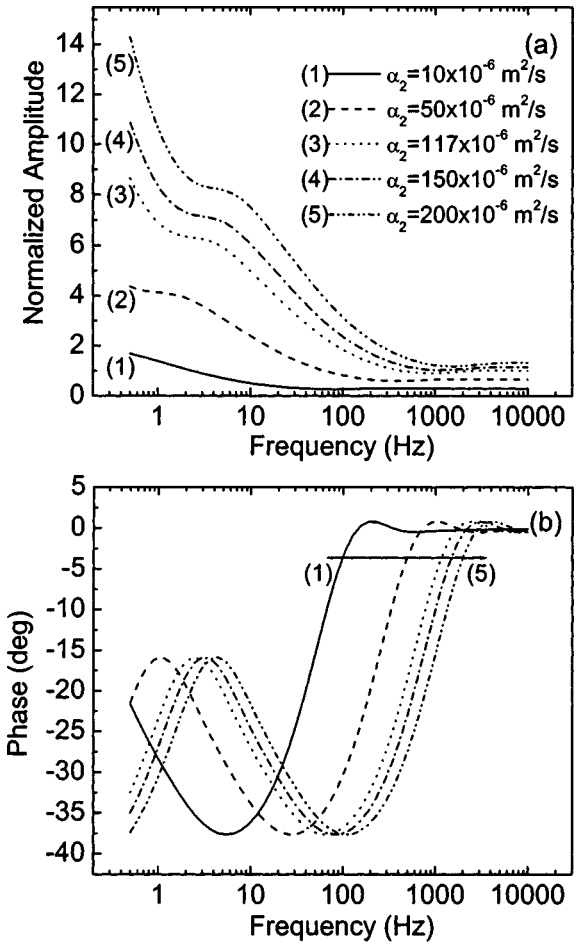

FIG. 6. Effect of the thermal diffusivity of a copper tube on the thermal-wave field. The interior and exterior radii of the tube are $a=2.1$ mm and $b=2.35$ mm, respectively. Thermal conductivity of the tube is assumed to be $401\ \mathrm{W/m\,K}$.

pattern (thermal standing wave) extremum shifts to higher frequencies and broadens, as expected. At frequencies $\sim$10 kHz, the effects of curvature become less pronounced due to the decreasing thermal diffusion length, with the result that the normalized phase difference tends to be zero as expected from planar structures. In this limit, the thermal wave in the wall is purely one dimensional in an effectively semi-infinite solid and Eq. (18) becomes valid, which also renders the amplitude ratio flat and equal to unity.

In order to see the difference between the exact and approximate calculations, the approximate calculation with $\eta_{1m}=0$ is also shown in Figs. 5(a) and 5(b) (empty squares). The approximate calculation is performed for the case of $a=2.2$ mm and $b=2.35$ mm only, to avoid overcrowding the plots. Detailed examination of the approximate and exact calculations in this and other simulations reveals that differences between the two results in both amplitude and phase appear in the second decimal place, which implies an excellent approximation. Therefore, for a hollow metallic tube, the thermal-wave field is only a function of tube dimension, and of thermal diffusivity and conductivity of the tube material. This conclusion provides a welcome simplicity for measuring thermophysical properties of hollow cylindrical samples.

The effect of the thermal diffusivity of the tube on the thermal-wave field is shown Fig. 6. Again, the signal is normalized with a semi-infinite copper sample with a flat surface, and the temperature is measured at $\varphi=90°$ and $\theta=180°$. The radii of the interior and exterior of the tube are $a=2.1$ mm and $b=2.35$ mm, respectively. The thermal conductivity of the tube is assumed to be $401\ \mathrm{W/m\,K}$. In a manner similar to that observed in Fig. 4(a), the normalized amplitude increases as the thermal diffusivity increases owing to the nominally independent nature of the conductivity and diffusivity parameters. The most important feature that can be seen from Fig. 6(b), common with Fig. 4, is that the positions of the thermal-wave phase interference extrema change very sensitively with the change in thermal diffusivity of the tube material, shifting to higher frequencies with increasing values of this parameter, as expected. The phase profile (shape), however, does not change. Detailed examination of the various phase curves in Fig. 6(b) shows that all the curves corresponding to different thermal diffusivities are shifted along the frequency axis by a factor which depends monotonically on the thermal diffusivity of the material. This

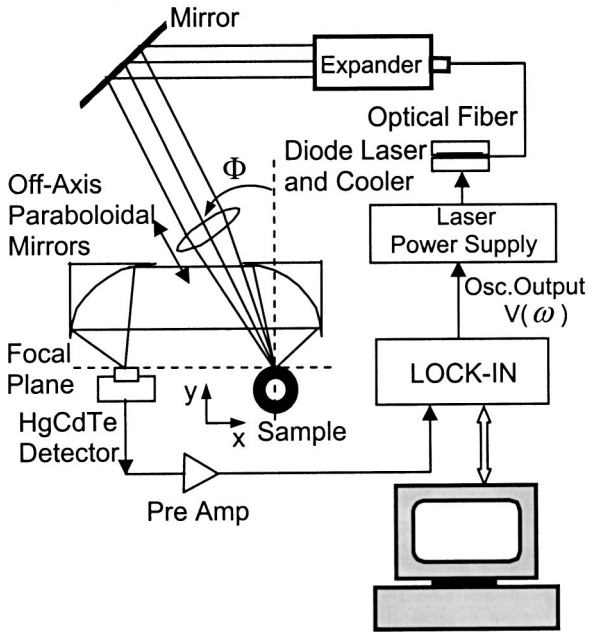

FIG. 7. Experimental setup for PTR of cylindrical solids.

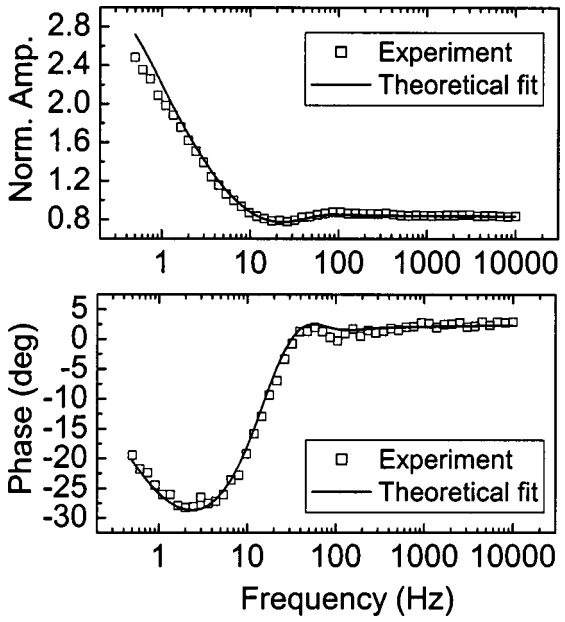

FIG. 8. Experimental and best-fit results (amplitude and phase) for a cylindrical stainless-steel tube (AISI 302) with interior and exterior diameters of 2.40 mm and 3.0 mm, respectively.

is a very important feature for measuring the thermal diffusivity of the tube material as it can be uniquely determined by the position of phase peak or trough.

As can be seen from Eq. (17), the thermal-wave field is also a function of the measurement angle φ. Although all the above simulations are calculated at $\varphi=90°$, the surface thermal-wave field measured by PTR depends on the measurement arrangement in practice. From the structure of Eq. (17), and in comparison with its one-layer analog in Ref. 7, Eq. (11), it is seen that the dependence of the thermal-wave field on the measurement angle φ is the same as that for homogeneous solids, which has been discussed in detail previously.[7] Nevertheless, for the sake of completeness, the measurement angle effect will be briefly addressed in the experimental section.

IV. EXPERIMENTAL RESULTS

In order to validate the theoretical model, PTR experiments were performed using a stainless-steel tube (AISI 302, composition: 0.15% C, 17%–19% Cr, 8%–10% Ni, and 2% Mn) with interior and exterior diameters of 2.4 and 3.0 mm, respectively. Tube-type hollow samples were chosen because (a) the sample structure is simple because the inner layer is air. For the purpose of validation of the theoretical model, the simpler the sample structure, the better the results, since fewer physical and geometrical parameters will be involved; (b) AISI 302 stainless-steel tubes are common products used as gas pipes, therefore, they are easy to obtain; and (c) the thermophysical properties of the material have been measured. Further applications of the model to cylindrical coating materials and hardened steel rods are in progress and will be reported later. The experimental setup is shown in Fig. 7. The thermal-wave optical source was a high-power semiconductor laser (Jenoptik JOLD-X-CPXL-1L ~10 W). The output of the laser was modulated by a periodic current driver (high-power laser diode driver, Thor Labs), the frequency of which was controlled by the computer and also served as the lock-in reference. The beam was expanded, collimated, and then focused onto the surface of the sample with a spot size ranging from ~1 to 21 mm by adjusting the position of the converging lens. The harmonically modulated infrared radiation from the sample surface was collected by an off-axis paraboloidal mirror system and detected by a HgCdTe detector (EG&G Judson Model J15016-M204-S204-S01M-WE-60). The signal from the detector was amplified by a low-noise preamplifier (EG&G Judson PA101) and then fed into a lock-in amplifier (EG&G Instruments, Model Model 7265) interfaced with a PC.

The experimental setup was initially optimized using a flat sample such that both sample and detector were on the focal plane of the off-axis mirrors as shown in Fig. 7. As already discussed elsewhere,[7] when the flat sample was replaced by a cylindrical surface, some adjustment had to be made such that the top point of the sample (i.e., the point tangential to the focal plane) was exactly placed (within experimental error) at the focal point of the paraboloidal mirror system. Therefore, the detector was monitoring the thermal-wave field emissions from this point. Thermal radiation information from other points of the sample would not be received by the detector, which is especially true for curved surfaces due to the strong defocusing (receding) effect of the curvature. After this adjustment, the laser beam was expanded to ~20 mm in diameter by moving the lens so that the laser beam was large enough to conform to the "infinite" z-axis illumination assumed in the model and also to validate the 1D model in the case of a flat sample. Figure 8 shows the experimental results and the corresponding theoretical fits for the aforementioned AISI 302 stainless-steel tube. The fitting was performed using the full expression Eq. (17) and the positions of the interferometric extrema in the phase frequency-scan curve. In the fitting process, the thermal dif-

fusivity of the tube material and the laser incidence angle φ are set as the only fitting parameters. The corresponding theoretical amplitude value in Fig. 8 was obtained using the values of these two fitted parameters as obtained from the phase channel without further adjustment. The only required input parameters for the fitting are the geometric dimensions of the tube, i.e., interior and exterior diameters. It is seen that both amplitude and phase show excellent agreement between experimental data and theoretical model best fits. The best-fitted AISI 302 steel thermal diffusivity in Fig. 8 was found to be 3.98×10^{-6} m^2/s, which is in excellent agreement with the literature value of 3.91×10^{-6} m^2/s for this type of steel.[13] Considering the experimental arrangement in which the laser beam is incident onto the sample at an angle Φ ($30°\sim35°$), Fig. 7, in the fitting process we also introduced the measurement angle φ as a fitting parameter to allow us to take into account this experimental factor. The best-fit angle result is $\varphi=57.3°$ (φ is as defined in Fig. 1) which translates into $\Phi=32.7°$ in Fig. 7, again, exhibiting very good agreement with the angle measured in the experimental setup.

V. CONCLUSIONS

We have formulated a thermal-wave model suitable for characterizing cylindrical composite (layered) structures using photothermal radiometry. Based on the derived Green functions for the two-layer cylindrical structures, the thermal-wave field from a cross section of an infinitely long two-layer cylinder was obtained. The physical characteristics of the thermal-wave field from coated cylindrical samples and hollow tubular samples have been discussed. As expected, the PTR signal of the coated cylindrical samples is a weighted contribution of both the interior and exterior materials depending on modulation frequency and thermal diffusivity which control the extent of the thermal probe length. It was found that both thermal conductivity and diffusivity of the coating affect the behavior of the PTR signal. However, only the thermal diffusivity affects the frequency positions of the thermal-wave field maxima and minima, especially in the phase channel. In the case of hollow opaque tubes (or tubes filled with low thermal-conductivity fluids), the PTR signal was further found to be dependent on the thermal diffusivity of the tube material only. The theoretical model was further tested through suitable experiments in which a cylindrical stainless-steel tube was examined using PTR and the frequency scans were compared to theoretical best fits, thus allowing the measurement of the thermal diffusivity of the steel. The latter was found to be in excellent agreement with literature values. This work offers a quantitative nondestructive PTR technique for thermophysical characterization of broad classes of composite cylindrical solids of industrial relevance (e.g., hardened steel rods, screws, pistons, etc.) which cannot be measured using flat sample geometries and plane thermal-wave theories.

ACKNOWLEDGMENT

The support of Materials and Manufacturing Ontario (MMO) through a Collaborative Contract is gratefully acknowledged.

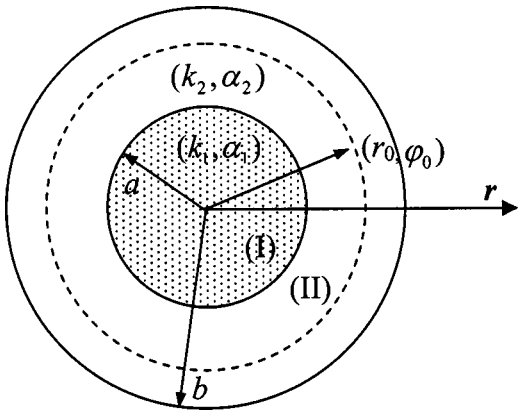

FIG. 9. Cross section of an infinitely long composite cylindrical solid consisting of two concentric regions of radii a (region I) and b (region II) with a spatially impulsive thermal-wave source at (r_0,φ_0), $a\leqslant r_0\leqslant b$.

APPENDIX

Section 1. Green function and spatial impulse-response functions for an infinitely long composite cylinder with a delta-function thermal-wave source at (r_0,φ_0), $a\leqslant r_0\leqslant b$, *Fig. 9. A homogeneous Neumann condition is prescribed at* $r=b$.

In region I with thermophysical properties (k_1,α_1), Fig. 9, the spatial thermal-wave impulse-response function, $H(\mathbf{r},\mathbf{r}_0;\omega)$, satisfies

$$\frac{1}{r}\frac{\partial}{\partial r}\left[r\frac{\partial}{\partial r}H(\mathbf{r},\mathbf{r}_0;\omega)\right]+\frac{1}{r^2}\frac{\partial^2}{\partial\varphi^2}H(\mathbf{r},\mathbf{r}_0;\omega)-\sigma_1{}^2(\omega)H(\mathbf{r},\mathbf{r}_0;\omega)=0. \tag{A1.1}$$

In region II with thermophysical properties (k_2,α_2), the Green function satisfies[8]

$$\frac{1}{r}\frac{\partial}{\partial r}\left[r\frac{\partial}{\partial r}G(\mathbf{r}|\mathbf{r}_0;\omega)\right]+\frac{1}{r^2}\frac{\partial^2}{\partial\varphi^2}G(\mathbf{r}|\mathbf{r}_0;\omega)-\sigma_2{}^2(\omega)G(\mathbf{r}|\mathbf{r}_0;\omega)=-\frac{\delta(r-r_0)\delta(\varphi-\varphi_0)}{\alpha_2 r}, \tag{A1.2}$$

where $\sigma_i=\sqrt{i\omega/\alpha_i}$, $(i=1,2)$. The polar Dirac delta function can be expanded as

$$\delta(\varphi-\varphi_0)=\frac{1}{2\pi}\sum_{m=-\infty}^{\infty}e^{im(\varphi-\varphi_0)}. \tag{A1.3}$$

Both Green function and impulse-response function in regions I and II can be expanded in the basis of the complete set of polar angle eigenfunctions $\{e^{im(\varphi-\varphi_0)}\}$:

$$G(\mathbf{r}|\mathbf{r}_0;\omega) = \frac{1}{2\pi}\sum_{m=-\infty}^{\infty} e^{im(\varphi-\varphi_0)} f_m(r,r_0), \tag{A1.4}$$

$$H(\mathbf{r},\mathbf{r}_0;\omega) = \frac{1}{2\pi}\sum_{m=-\infty}^{\infty} e^{im(\varphi-\varphi_0)} R_n(r,r_0). \tag{A1.5}$$

Substituting Eq. (A1.5) into Eq. (A1.1), we obtain for the radial function

$$\frac{1}{r}\frac{d}{dr}\left[r\frac{\partial}{\partial r}R_n(r,r_0)\right] - \left[\sigma_1{}^2(\omega) + \frac{n^2}{r^2}\right]R_n(r,r_0) = 0. \tag{A1.6}$$

The solution for the above equation is

$$R_n(r,r_0) = a_n I_n(\sigma_1 r) \quad (r \leqslant a). \tag{A1.7}$$

Similarly, substituting Eq. (A1.4) into Eq. (A1.2) and taking Eq. (A1.3) into account, we obtain for the radial function

$$\frac{1}{r}\frac{d}{dr}\left[r\frac{\partial}{\partial r}f_m(r,r_0)\right] - \left[\sigma_2{}^2(\omega) + \frac{m^2}{r^2}\right]f_m(r,r_0) = -\frac{\delta(r-r_0)}{\alpha_2 r}. \tag{A1.8}$$

The homogeneous solution of Eq. (A1.8) is

$$f_m(r,r_0) = \begin{cases} b_m I_m(\sigma_2 r) + c_m K_m(\sigma_2 r) & (a \leqslant r \leqslant r_0), \\ d_m I_m(\sigma_2 r) + e_m K_m(\sigma_2 r) & (r_0 \leqslant r \leqslant b) \end{cases} \tag{A1.9}$$

where $I_m(z)$, $K_m(z)$ are the complex-argument modified Bessel functions of the first kind and of the second kind of order m, respectively. To solve for the constants a_m, b_m, c_m, d_m, and e_m in Eqs. (A1.7) and (A1.9), the following boundary conditions are employed. At $r=r_0$,

$$f_m(r,r_0)|_{r=r_0^+} = f_m(r,r_0)|_{r=r_0^-}, \tag{A1.10}$$

$$\frac{d}{dr} f_m(r,r_0)|_{r=r_0^+} - \frac{d}{dr} f_m(r,r_0)|_{r=r_0^-} = -\frac{1}{\alpha_2 r_0}. \tag{A1.11}$$

At $r=a$, thermal-wave field and flux continuity conditions apply

$$H(\mathbf{r},\mathbf{r}_0;\omega)|_{r=a} = G(\mathbf{r}|\mathbf{r}_0;\omega)|_{r=a}, \tag{A1.12}$$

$$k_1\frac{\partial H(\mathbf{r},\mathbf{r}_0;\omega)}{\partial r}\bigg|_{r=a} = k_2\frac{\partial G(\mathbf{r}|\mathbf{r}_0;\omega)}{\partial r}\bigg|_{r=a}. \tag{A1.13}$$

At $r=b$, the adiabatic (homogeneous) Neumann condition is assumed

$$\frac{\partial G(\mathbf{r}|\mathbf{r}_0;\omega)}{\partial r}\bigg|_{r=b} = 0. \tag{A1.14}$$

Solving Eqs. (A1.10), (A1.11), (A1.12), (A1.13), and (A1.14) using Eqs. (A1.7) and (A1.9), we find

$$a_m = \left(\frac{\beta_{21}}{\alpha_2 a}\right)\frac{[I_m(\sigma_2 r_0)K_m'(\sigma_2 b) - I_m'(\sigma_2 b)K_m(\sigma_2 r_0)]}{Z(a,b)}, \tag{A1.15}$$

$$b_m = -\left(\frac{p(a)}{\alpha_2}\right)\frac{[I_m(\sigma_2 r_0)K_m'(\sigma_2 b) - I_m'(\sigma_2 b)K_m(\sigma_2 r_0)]}{Z(a,b)}, \tag{A1.16}$$

$$c_m = \left(\frac{g(a)}{\alpha_2}\right)\frac{[I_m(\sigma_2 r_0)K_m'(\sigma_2 b) - I_m'(\sigma_2 b)K_m(\sigma_2 r_0)]}{Z(a,b)}, \tag{A1.17}$$

$$d_m = -\left(\frac{K_m'(\sigma_2 b)}{\alpha_2}\right)\frac{[p(a)I_m(\sigma_2 r_0) - g(a)K_m(\sigma_2 r_0)]}{Z(a,b)}, \tag{A1.18}$$

$$e_m = \left(\frac{I_m'(\sigma_2 b)}{\alpha_2}\right)\frac{[p(a)I_m(\sigma_2 r_0) - g(a)K_m(\sigma_2 r_0)]}{Z(a,b)}, \tag{A1.19}$$

where the various primes indicate derivatives as defined in Eqs. (A1.25), (A1.26), (A1.27), and (A1.28) below. Additional definitions of special functions are as follows:

$$p(a) \equiv \beta_{21} I_m(\sigma_1 a)K_m'(\sigma_2 a) - I_m'(\sigma_1 a)K_m(\sigma_2 a), \tag{A1.20}$$

$$g(a) \equiv \beta_{21} I_m(\sigma_1 a)I_m'(\sigma_2 a) - I_m'(\sigma_1 a)I_m(\sigma_2 a), \tag{A1.21}$$

$$Z(a,b) \equiv p(a)I_m'(\sigma_2 b) - g(a)K_m'(\sigma_2 b), \tag{A1.22}$$

with

$$\beta_{21} \equiv k_2/k_1 \quad b_{21} \equiv k_2\sigma_2/k_1\sigma_1. \tag{A1.22b}$$

Finally, the Green function in region II can be expressed as

$$G(\mathbf{r}|\mathbf{r}_0;\omega) = \frac{1}{2\pi\alpha_2}\sum_{m=-\infty}^{\infty}\frac{e^{im(\varphi-\varphi_0)}}{Z(a,b)} \times \begin{cases} -K_m'(\sigma_2 b)[p(a)I_m(\sigma_2 r) - g(a)K_m(\sigma_2 r)]I_m(\sigma_2 r_0) + I_m'(\sigma_2 b)[p(a)I_m(\sigma_2 r) - g(a)K_m(\sigma_2 r)]K_m(\sigma_2 r_0) & (a \leqslant r \leqslant r_0) \\ -K_m'(\sigma_2 b)[p(a)I_m(\sigma_2 r_0) - g(a)K_m(\sigma_2 r_0)]I_m(\sigma_2 r) + I_m'(\sigma_2 b)[p(a)I_m(\sigma_2 r_0) - g(a)K_m(\sigma_2 r_0)]K_m(\sigma_2 r) & (r_0 \leqslant r \leqslant b) \end{cases}. \tag{A1.23}$$

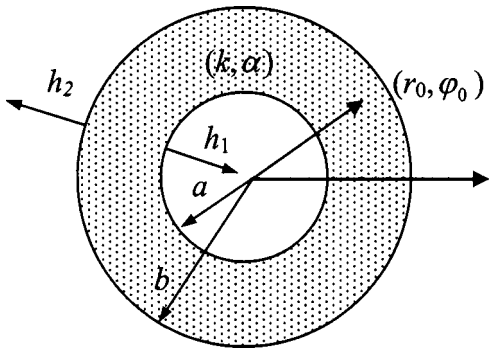

FIG. 10. Cross section of an infinitely long hollow cylinder of radii a (region I) and b (region II) with a spatially impulsive thermal-wave source at (r_0,φ_0), $a\leqslant r_0\leqslant b$.

The impulse-response function in region (I) is

$$H(\mathbf{r},\mathbf{r}_0;\omega)=\frac{\beta_{21}}{2\pi\alpha_2 a}\sum_{n=-\infty}^{\infty}\frac{e^{in(\varphi-\varphi_0)}}{Z(a,b)}[I_n(\sigma_2 r_0)K_n'(\sigma_2 b) - I_n'(\sigma_2 b)K_n(\sigma_2 r_0)]I_n(\sigma_1 r)\quad(0\leqslant r\leqslant a). \tag{A1.24}$$

The following definitions and recursion relations for any integer or noninteger ν are employed during the derivation of the Green function and impulse-response function:[10]

$$I_\nu'(\sigma r_0)=\frac{d}{dr}\,I_\nu(\sigma r)\big|_{r=r_0}, \tag{A1.25}$$

$$I_\nu'(\sigma r_0)=\sigma I_{\nu+1}(\sigma r_0)+\frac{\nu}{r_0}I_\nu(\sigma r_0), \tag{A1.26}$$

$$K_\nu'(\sigma r_0)=-\sigma K_{\nu+1}(\sigma r_0)+\frac{\nu}{r_0}K_\nu(\sigma r_0). \tag{A1.27}$$

The Wronskian formula

$$I_\nu'(\sigma r_0)K_\nu(\sigma r_0)-I_\nu(\sigma r_0)K_\nu'(\sigma r_0)=\frac{1}{r_0} \tag{A1.28}$$

is very useful for simplifying products of modified Bessel functions and their derivatives especially in the denominator of the Green function and impulse-response function.

Section 2. Green function for an infinitely long hollow cylinder with a delta-function thermal-wave source at (r_0,φ_0), $a\leqslant r_0\leqslant b$, *Fig. 10. Third-kind boundary conditions are prescribed at both* $r=a$ *and* $r=b$.

In region $a\leqslant r\leqslant b$, the Green function satisfies[8]

$$\frac{1}{r}\frac{\partial}{\partial r}\left[r\frac{\partial}{\partial r}G(\mathbf{r}|\mathbf{r}_0;\omega)\right]+\frac{1}{r^2}\frac{\partial^2}{\partial\varphi^2}G(\mathbf{r}|\mathbf{r}_0;\omega)-\sigma^2(\omega)G(\mathbf{r}|\mathbf{r}_0;\omega) =-\frac{\delta(r-r_0)\delta(\varphi-\varphi_0)}{\alpha r}. \tag{A2.1}$$

The polar Dirac delta function can be expanded as

$$\delta(\varphi-\varphi_0)=\frac{1}{2\pi}\sum_{m=-\infty}^{\infty}e^{im(\varphi-\varphi_0)}. \tag{A2.2}$$

The Green function can be expanded in the basis of the complete set of polar angle eigenfunctions $\{e^{im(\varphi-\varphi_0)}\}$:

$$G(\mathbf{r}|\mathbf{r}_0;\omega)=\frac{1}{2\pi}\sum_{m=-\infty}^{\infty}e^{im(\varphi-\varphi_0)}f_m(r,r_0). \tag{A2.3}$$

Substituting Eq. (A2.3) into (A2.1) and taking Eq. (A2.2) into account, we find that f_m must satisfy the equation

$$\frac{1}{r}\frac{d}{dr}\left[r\frac{\partial}{\partial r}f_m(r,r_0)\right]-\left[\sigma^2(\omega)+\frac{m^2}{r^2}\right]f_m(r,r_0) =-\frac{\delta(r-r_0)}{\alpha r}. \tag{A2.4}$$

The homogeneous solution of Eq. (A2.4) is

$$f_m(r,r_0)=\begin{cases}b_m I_m(\sigma r)+c_m K_m(\sigma r) & (a\leqslant r\leqslant r_0)\\ d_m I_m(\sigma r)+e_m K_m(\sigma r) & (r_0\leqslant r\leqslant b)\end{cases}. \tag{A2.5}$$

To solve the constants b_m, c_m, d_m, and e_m in Eq. (A5), the following boundary conditions are employed:

At $r=r_0$, continuity of Green function and discontinuity of its derivative

$$f_m(r,r_0)|_{r=r_0^+}=f_m(r,r_0)|_{r=r_0^-}, \tag{A2.6}$$

$$\frac{d}{dr}f_m(r,r_0)|_{r=r_0^+}-\frac{d}{dr}f_m(r,r_0)|_{r=r_0^-}=-\frac{1}{\alpha r_0}. \tag{A2.7}$$

Homogeneous boundary conditions at $r=a$:

$$k\left.\frac{\partial f_m(r,r_0)}{\partial r}\right|_{r=a}=h_1 f_m(r,r_0)|_{r=a}, \tag{A2.8}$$

and at $r=b$:

$$-k\left.\frac{\partial f_m(r,r_0)}{\partial r}\right|_{r=b}=h_2 f_m(r,r_0)|_{r=b}. \tag{A2.9}$$

Now solving Eqs. (A2.6), (A2.7), (A2.8), and (A2.9), we obtain

$$b_m=\left(\frac{X_m(a)}{\alpha}\right)\frac{[K_m(\sigma r_0)-Y_m(b)I_m(\sigma_2 r_0)]}{[Y_m(b)-X_m(a)]}, \tag{A2.10}$$

$$c_m=\left(\frac{1}{\alpha}\right)\frac{[K_m(\sigma r_0)-Y_m(b)I_m(\sigma r_0)]}{[Y_m(b)-X_m(a)]}, \tag{A2.11}$$

$$d_m=\left(\frac{Y_m(b)}{\alpha}\right)\frac{[K_m(\sigma r_0)-X_m(a)I_m(\sigma_2 r_0)]}{[Y_m(b)-X_m(a)]}, \tag{A2.12}$$

$$e_m=\left(\frac{1}{\alpha}\right)\frac{[K_m(\sigma r_0)-X_m(a)I_m(\sigma r_0)]}{[Y_m(b)-X_m(a)]}, \tag{A2.13}$$

where the following function definitions were used:

$$X_m(a)\equiv\frac{K_m'(\sigma a)-m_1K_m(\sigma a)}{I_m'(\sigma a)-m_1I_m(\sigma a)}, \tag{A2.14}$$

$$Y_m(b)\equiv\frac{K_m'(\sigma b)-m_2K_m(\sigma b)}{I_m'(\sigma b)-m_2I_m(\sigma b)}, \tag{A2.15}$$

with

$$m_1 \equiv h_1/k \quad m_2 \equiv h_2/k. \tag{A2.15b}$$

Finally, the Green function can be expressed as

$$G(\mathbf{r}|\mathbf{r}_0;\omega) = \frac{1}{2\pi\alpha}\sum_{m=-\infty}^{\infty}\frac{e^{im(\varphi-\varphi_0)}}{[Y_m(b)-X_m(a)]} \times \begin{cases} K_m(\sigma r_0)[K_m(\sigma r)-X_m(a)I_m(\sigma r)] - Y_m(b)I_m(\sigma r_0)[K_m(\sigma r)-X_m(a)I_m(\sigma r)] & (a \leqslant r \leqslant r_0) \\ K_m(\sigma r)[K_m(\sigma r_0)-X_m(a)I_m(\sigma r_0)] - Y_m(b)I_m(\sigma r)[K_m(\sigma r_0)-X_m(a)I_m(\sigma r_0)] & (r_0 \leqslant r \leqslant b) \end{cases}. \tag{A2.16}$$

Section 3. Equivalence between a two-layer composite cylinder with a homogeneous Neumann condition at the exterior surface ($r=b$) *(Sec. I) and a hollow cylinder (Sec. II) with a homogeneous Neumann condition at* $r=b$ *(exterior surface) and a homogeneous third-kind boundary condition at* $r=a$ *(interior surface).*

In Sec. I, the impulse-response function, Eq. (A1.23), evaluated at $r=a$ can be rearranged as follows:

$$G(a|r_0;\omega) = \frac{1}{2\pi\alpha_2}\sum_{m=-\infty}^{\infty} e^{im(\varphi-\varphi_0)} \times \frac{\frac{1}{a}[I'_m(\sigma_2 b)K_m(\sigma_2 r_0) - K'_m(\sigma_2 b)I_m(\sigma_2 r_0)]}{[I'_m(\sigma_2 a)K'_m(\sigma_2 b) - I'_m(\sigma_2 b)K'_m(\sigma_2 a)] + \frac{I'_m(\sigma_1 a)}{\beta_{21}I_m(\sigma_1 a)}[I'_m(\sigma_2 b)K_m(\sigma_2 a) - I_m(\sigma_2 a)K'_m(\sigma_2 b)]}. \tag{A3.1}$$

In Sec. II, the Green function at $r=a$ can also be rearranged assuming $m_2=0$ corresponding to a homogeneous Neumann condition at the exterior surface, in order to compare it with the case in Sec. I

$$G(a|r_0;\omega) = \frac{1}{2\pi\alpha_2}\sum_{m=-\infty}^{\infty} e^{im(\varphi-\varphi_0)} \times \frac{\frac{1}{a}[I'_m(\sigma_2 b)K_m(\sigma_2 r_0) - K'_m(\sigma_2 b)I_m(\sigma_2 r_0)]}{[I'_m(\sigma_2 a)K'_m(\sigma_2 b) - I'_m(\sigma_2 b)K'_m(\sigma_2 a)] + m_1[I'_m(\sigma_2 b)K_m(\sigma_2 a) - I_m(\sigma_2 a)K'_m(\sigma_2 b)]}. \tag{A3.2}$$

Comparing Eq. (A3.1) and (A3.2), we find the following equivalence relations;

$$m_1 = \frac{I'_m(\sigma_1 a)}{\beta_{21}I_m(\sigma_1 a)} \tag{A3.3}$$

and

$$h_1 = \frac{k_1 I'_m(\sigma_1 a)}{I_m(\sigma_1 a)}. \tag{A3.4}$$

On replacing the otherwise arbitrary constants m_1 and h_1 in Eq. (A1.23) with the foregoing expressions which contain thermal-wave parameters from the underlayer region I, the impulse-response function (A1.23) can be transformed into an *improper* Green function for region II. As such, Eq. (A1.23) with (A3.3) and (A3.4) satisfies the field Eq. (5) with those particular values of m_1 and h_1.

[1] *Principles and Perspectives of Photothermal and Photoacoustic Phenomena*, in Progress in Photothermal and Photoacoustic Science and Technology Vol. 1, edited by A. Mandelis (North-Holland, New York, 1991).
[2] *Non-Destructive Evaluation*, in Progress in Photothermal and Photoacoustic Science and Technology Vol. 2, edited by A. Mandelis (PTR Prentice Hall, Englewood Cliffs, NJ, 1993).
[3] L. A. Skvortsov and V. M. Kirillov, Quantum Electron. **33**, 1113 (2003).
[4] A. Ocariz, A. Sanchez-Lavega, and R. Celorrio, J. Appl. Phys. **81**, 7552 (1997).
[5] H. K. Park, C. P. Grigoropoulos, and A. C. Tam, Int. J. Thermophys. **16**, 973 (1995).
[6] A. Salazar, A. Sanchez-Lavega, and J. M. Terron, J. Appl. Phys. **84**, 3031 (1998).
[7] C. Wang, A. Mandelis, and Y. Liu, J. Appl. Phys. **96**, 3756 (2004).
[8] A. Mandelis, *Diffusion-Wave Fields: Mathematical Methods and Green Functions* (Springer, New York, 2001), Chap. 6, p. 413.
[9] A. Rosencwaig and A. Gersho, J. Appl. Phys. **47**, 64 (1976).
[10] *Handbook of Mathematical Functions*, National Bureau of Standards Appl. Math Ser. 55 edited by M. Abramowitz and I. A. Stegun (Dover, New york, 1964).
[11] A. Mandelis, *Diffusion-Wave Fields: Mathematical Methods and Green Functions* (Springer, New York, 2001), Chap. 2.3, p. 90.
[12] *Properties of Selection: Iron, Steel of High Performance Alloys*, Vol. 1, in *Metal Handbook*, 10th ed. (ASM International, Material Park, Ohio, 1990), p. 196.
[13] F. P. Incropera, *Fundamentals of Heat and Mass Transfer*, 3rd ed. (Wiley, New York, 1990), p. A3.